

Complete state tomography of a quantum dot confined spin qubit.

Dan Cogan,¹ Giora Peniakov,¹ Zu-En Su,¹ and David Gershoni^{1,*}

¹*The Physics Department and the Solid State Institute,
Technion-Israel Institute of Technology, 3200003 Haifa, Israel*

Semiconductor quantum dots are probably the preferred choice for interfacing anchored, matter spin qubits and flying photonic qubits. While full tomography of a flying qubit or light polarization is in general straightforward, matter spin tomography is a challenging and resource-consuming task. Here we present a novel all-optical method for conducting full tomography of quantum-dot-confined spins. Our method is applicable for electronic spin configurations such as the conduction-band electron, the valence-band hole, and for electron-hole pairs such as the bright and the dark exciton. We excite the spin qubit using short resonantly tuned, polarized optical pulse, which coherently converts the qubit to an excited qubit that decays by emitting a polarized single-photon. We perform the tomography by using two different orthogonal, linearly polarized excitations, followed by time-resolved measurements of the degree of circular polarization of the emitted light from the decaying excited qubit. We demonstrate our method on the dark exciton spin state with fidelity of 0.94, mainly limited by the accuracy of our polarization analyzers.

I. INTRODUCTION

Qubits are the building blocks of quantum technologies [1, 2]. Qubits can be realized in many physical two-level systems, which maintain their coherence for a much longer time than the time required to initialize their coherent states, read, or subject the state to logical gates [3–6]. The vision of quantum technologies is frequently described in terms of anchored qubits, located on different nodes in space where they serve as quantum information processors or quantum memories, and flying qubits that propagate long distances, connecting the various nodes[7]. Photons are natural flying qubits since they can travel long distances without dephasing, while their polarization state carries the quantum information [8, 9]. The spins of single electrons, nuclei, atoms or molecules are examples for anchored qubits. In some instances, they can be isolated, thereby maintaining spin coherence for very long times [4, 10–13]. Semiconductor quantum dots are an excellent interface between anchored spin qubits and flying photonic qubits due to their ability to both isolate electronic spin qubits and to enhance their interaction with the photons light field. Quantum photonic devices based on semiconductor quantum dots, such as described in Fig. 1a, are almost ideally suited for building highly-performant, optically-active quantum nodes.

Determining the qubit state generally requires projections on various basis states in a process called tomography. Full tomography of the polarization state of flying photonic qubits is quite straightforwardly done using state of the art polarizers and retarders [14, 15]. Researchers have developed methods for measuring matter qubits' spin in various systems [16–20]. Full tomography of confined spin qubits in semiconductor QDs remains however, challenging and demanding [21, 22]. These dif-

ficulties are reflected in the various methods, developed in recent years, which require application of relatively strong magnetic fields. The fields affect the qubits and alter their energy level structure [23–25], rendering the spin tomography inaccurate.

Relevant to this work is the all-optical method developed by Benny et al. [26], demonstrating full tomography of a QD confined bright exciton (BE - an electron-hole pair) spin. The bright exciton is a spin integer quasi-particle, with a total angular projection of either +1 or -1 on the QD symmetry axis. This nondegenerate spin qubit forms an optical Λ -system with the spin-zero biexciton state, which results from resonant optical excitation of the BE, as schematically described in Fig. 1b. In this optical Λ -system, each of the BE qubit's two states is optically connected to the biexciton single state. A non-degenerate qubit, which is part of an optical Λ -system facilitates a relatively easy way for optical spin tomography, resulting from a one-to-one correspondence between the polarization of the spin and the photon, inducing the optical transition. A nondegenerate spin qubit naturally precesses in time, and therefore, time-resolved polarization-sensitive spectroscopy can be used for full tomography of the precessing spin qubit [26].

The situation is different for a QD confined single-charge carrier such as the conduction-band electron or the valence-band hole. A charge carrier has a half-integer spin, and as such in the absence of an external magnetic field, the qubit that it forms is Kramers' degenerate. Similarly, an optically excited charge carrier (positive or negative trion), is also a Kramers' degenerate half-integer spin state. Therefore, the charge and the excited charge are both spin qubits that form an optical Π -system rather than a Λ -system as can be seen in Fig. 1c. The conduction-band electron [1, 2, 27], the valence-band hole [28, 29], and the dark exciton (DE- optically inactive electron-hole pair)[30–32] are long-lived ground electronic spin qubits in a QD system. The first two are Kramers' degenerate, but the third one is not. All three qubits form a natural Π -system with circularly polarized

* dg@physics.technion.ac.il

optical selection rules to their excited qubits [13]. Thus, tomography as in the BE case [26] is impossible.

One way to circumvent this problem as described in Fig. 1d is to apply a strong magnetic field, which lifts the Kramers' degeneracy of the optically excited spin state, thereby facilitating an optical Λ -like system between the carrier's spin states and one of the optically excited states [23, 24, 33]. However, the strong magnetic field also lifts the degeneracy of the ground level qubit, thus creating a spectral "which path" information for the emitted photons. Therefore, the use of this artificially-created Λ -system for spin-photon entanglement [24, 25], requires erasing the spectral or the polarization information encoded in the emitted photon, thereby limiting the method applicability and scalability.

Here, we develop and demonstrate a novel, all-optical spin tomography method, which uses the natural Π -system that the spin qubit is a part of, for the optical tomography. The method is general, accurate, and can be applied for state-tomography of multi-qubits, and entangled spin-photon states [34–36]. For Kramers' degenerate spin qubits, however, a minimal external magnetic field in Voigt configuration is still required for lifting the degeneracy and induce spin precession. We perform the tomography in the following way: first, we excite the spin qubit under study, which we call the ground level qubit, to an optically active excited qubit state, which we call the excited qubit. This coherent and deterministic conversion is done using a short resonantly-tuned linearly-polarized optical π -pulse, such that there is a one-to-one correspondence between the state of the ground level qubit and that of the excited qubit. The excited qubit then radiatively recombines while its spin state evolves during the recombination in a frequency given by the energy difference between the excited qubit eigenstates. The Π -system optical selection rules are such that by using time-resolved circular polarization-sensitive PL spectroscopy one can trace back the state of the excited qubit at the moment of conversion, and in turn the state of the ground level qubit, prior to the conversion pulse. Full tomography is obtained using two conversions on two different linear polarization bases.

Unlike the single charge carriers, the DE is an integer spin qubit [30, 31], its eigenstates are not degenerate, and thus even in the absence of an external magnetic field, the DE qubit naturally precesses. In addition, the DE spin state can be written-up as any desired coherent superposition of its eigenstates by a single, picosecond long optical pulse [32]. Therefore, we demonstrate the tomography on the DE spin qubit, though the method applies to single-charge carriers as well.

II. EXPERIMENT

Typical size of an epitaxially grown semiconductor QD is tens of nanometers in diameter, and a few nanometers in height, forming a 3D potential trap that confines

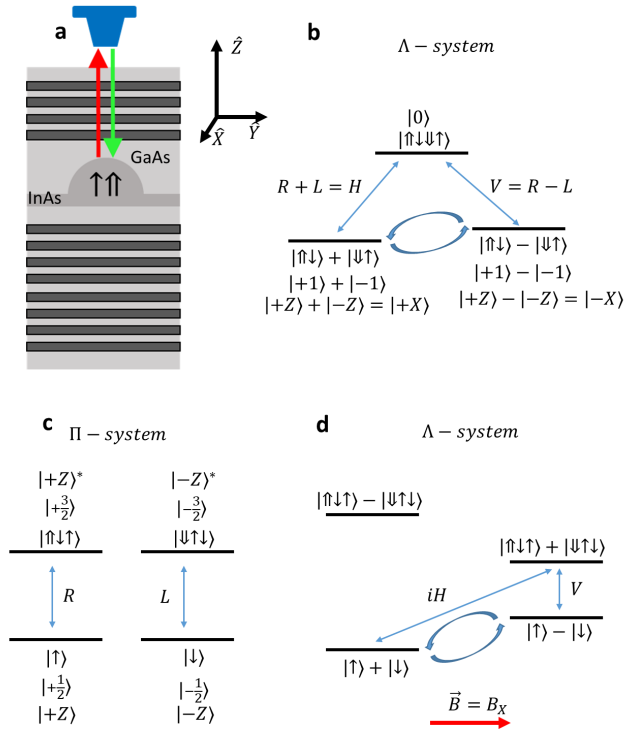


Figure 1. a) Schematic description of the studied single QD device. The QD is located in the focal point of a microscope objective, which focuses the pulsed laser beam (represented by a green arrow) and collimates the emitted PL (red arrow). Here \hat{z} defines the growth direction of the QD. b) schematic description of the confined BE - biexciton as an optical Λ -system and c) the confined electron -trion as an optical Π -system. d) Transforming an optical Π -system into a Λ -system using an external magnetic field. Here \uparrow (\downarrow) represents spin-up electron (spin-down hole) and R and L represent right and left hand circularly polarized optical transition. Numbers indicate the total angular momentum of the electronic state. Here $||+Z\rangle$ ($|-Z\rangle^*$) represent spin up ground (spin down excited) state along the \hat{z} axis, and $||+X\rangle$ ($|-X\rangle^*$) represent coherent superpositions as defined in the figure.

electrons, holes, and electron-hole pairs (excitons). Figure 1a illustrates the QD device used in this work. The InAs layer of the QDs is embedded in a GaAs optical microcavity formed by 2 Bragg reflecting mirrors of Al-GaAs/GaAs. The role of the microcavity is to increase the harvesting efficiency of the light emitted from the QD [37]. A microscope objective with a numerical aperture of 0.8 is used to both focus the laser pulses on a single QD, and to collect the single photons emitted. A QD confined dark exciton (DE) is composed of a conduction-band electron and a valence-band hole pair, with parallel spins [30, 31]. It is called dark since the two carriers cannot recombine radiatively due to their electronic spin mismatch. This fact is also reflected in the DE total

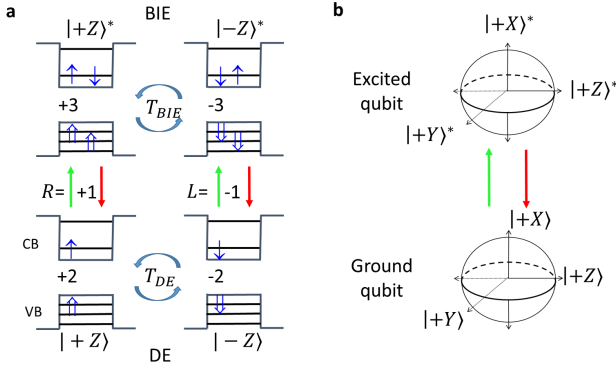


Figure 2. a) Energy levels, spin wavefunctions, and polarization selection rules for resonant optical transitions for the QD confined dark exciton (DE) and the optical P-system that it forms with its optically excited biexciton (BIE). (b) Bloch sphere representation of the confined ground spin qubit and the excited spin qubit. Here $|+Z\rangle$ ($|-Z\rangle^*$) represent spin up ground (spin down excited) state along the \hat{z} axis, and $|+X\rangle$ ($|-X\rangle^*$) and $|+Y\rangle$ ($|-Y\rangle^*$) represent coherent superpositions.

angular momentum projection of ± 2 which can not be carried out by a single photon, possessing an angular momentum of ± 1 , only. Consequently, the QD confined DE forms a spin qubit which has orders of magnitude longer lifetime than the BE [31].

The DE can be optically excited by absorbing a photon, thereby photogenerating an additional electron-hole pair in the QD. Resonant excitation of the DE as schematically described in Fig. 2a will result in an excited biexcitonic spin qubit (BIE). The BIE is a four carrier state comprised of two anti-parallel electron spins forming a singlet in the lowest conduction band level and two heavy-holes with parallel spins, forming a triplet, where one hole is in the valence bands' ground energy level, and the other one is in the first excited energy level. The total angular momentum of the BIE is ± 3 , given by the total spin projection of the two unpaired holes. Figure 2b illustrates the Bloch sphere representation of the confined ground spin qubit and the excited spin state. $|+Z\rangle$ ($|-Z\rangle^*$) represent spin up ground (spin down excited) state along the \hat{z} axis, defined by the growth direction of the QD, and $|+X\rangle$ ($|-X\rangle^*$) and $|+Y\rangle$ ($|-Y\rangle^*$) represent coherent superpositions as illustrated in the figure. After photogeneration, in about 0.5 ns, the excited spin decays radiatively by emitting a photon. One note in Fig. 1c, and Fig. 2b that the ground and excited qubit form an optical Π -system, in which right (left) hand circularly polarized optical transitions connect the $|+Z\rangle$ ($|-Z\rangle$) states of the ground and excited qubits.

We use a linearly polarized resonant optical π -pulse to convert the ground qubit coherently and deterministically to the excited qubit, with a one-to-one correspondence between the two states. The excited qubit then

radiatively decays while its spin state evolves during the relaxation. The selection rules of the optical Π -system are such that a spin-up state of the excited qubit ($|Z\rangle^*$) results in the emission of a right hand circularly polarized photon while a spin-down state ($|-Z\rangle^*$) results in the emission of a left hand circularly polarized photon. Thus, by using time-resolved circularly polarized sensitive PL spectroscopy one can trace back the state of the excited qubit at the moment of conversion, and in turn the state of the ground-level qubit, prior to the conversion.

Fig. 3 describes the procedure for full state tomography. The central Bloch sphere describes a general ground-level-qubit state as a coherent superposition of the two $|\pm Z\rangle$ states. Likewise, the outer Bloch spheres describe the states of the excited qubit as a superposition of the $|\pm Z^*\rangle$ states, following the optical pulse conversions, for four different pulse polarizations.

In Fig. 3, as in Fig. 2, the green arrow describes the π -pulse which converts the ground-level-qubit to the excited-qubit, while the red arrow describes single-photon emission resulting from the excited-qubit recombination. The ground spin state in Fig. 3 is defined on the central Bloch sphere by the vector:

$$\vec{S}^0 = [S_X^0, S_Y^0, S_Z^0].$$

\vec{S}^0 is the spin-state that one measures by state tomography. This state is converted to the excited qubit by applying a polarized 12-ps long π -pulse, energetically tuned to the ground-level – excited-level optical transition. Since in this Π -system $|R\rangle$ photons connect only between $|+Z\rangle$ to $|+Z^*\rangle$ states, while $|L\rangle$ photons connect only between $|-Z\rangle$ to $|-Z^*\rangle$ states, it follows that R- (L-) circularly polarized conversion pulse, successfully applied to the ground-level-qubit results in an excited qubit initial state which is given by $\vec{S}^{*,0,R(L)} = [0, 0, \pm 1]$ as shown in Fig. 3a (b). These two circularly polarized conversion pulses always initialize the excited-qubit to the same states from any initial ground-level-qubit state. However, when the conversion pulses are linearly polarized, the situation is different. $|H\rangle = 1/\sqrt{2}(|R\rangle + |L\rangle)$ polarized pulse converts the ground-spin state to the same excited-spin state and $|B\rangle = 1/\sqrt{2}\exp(-i\pi/4)(|R\rangle + i|L\rangle)$ linearly polarized pulse also rotates the excited-spin phase by 90° around the z-axis. Thus, after H conversion, the initial state of the excited-qubit is given by:

$$\vec{S}^{*,0,H} = [S_X^0, S_Y^0, S_Z^0], \quad (1)$$

as shown in Fig. 3c and after B conversion, the initial state is:

$$\vec{S}^{*,0,B} = [-S_Y^0, S_X^0, S_Z^0], \quad (2)$$

as shown in Fig. 3d.

Following the conversion the initial excited-qubit state evolves in time by precessing around the eigenstates-axis

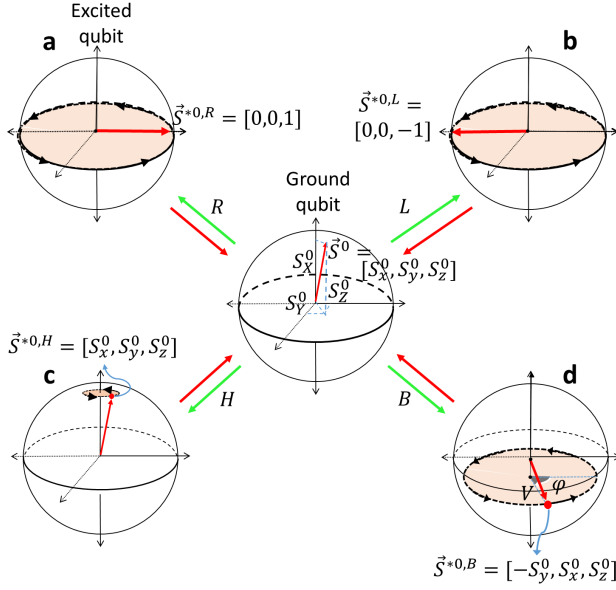


Figure 3. Schematic description of the spin-state tomography. The red arrow on the central Bloch sphere represents the confined ground-level spin-state, described by the vector $\vec{S}^0 = [S_x^0, S_y^0, S_z^0]$. A polarized optical π -pulse (green arrow) converts the ground spin qubit into the excited qubit. The excited qubit evolves in time while it radiatively recombines and emits a single photon (red arrow). Figures (a)-(d) describe four different polarizations of the converting pulse: (a) R-conversion, (b) L-conversion, (c) H-conversion, and (d) B-conversion. In each case, the red arrow on the excited-qubit Bloch sphere describes the excited-qubit state at the moment of conversion and the direction of the state's precession. The amplitude V^0 and the time-dependent phase $\varphi(t)$ characterize this precession. While R (L) circularly polarized excitation initializes the excited qubit in its $|+Z\rangle$ ($|-Z\rangle$) spin-state, H (B) polarized excitation maintains the phase information of the ground qubit and converts it to $S^{*0,H} = [S_x^0, S_y^0, S_z^0]$, ($S^{*0,B} = [-S_y^0, S_x^0, S_z^0]$).

(X) with a time period $T_{excited}$. The precessing state projection on the Z-axis of the excited-qubit Bloch sphere is therefore given by:

$$S_Z^*(t) = V^0 \cos\left(-\frac{2\pi t}{T_{excited}} + \varphi^0\right), \quad (3)$$

where V^0 and φ^0 are defined as the amplitude and phase. Here, for R conversion

$$V^0 = V_R^0 = 1; \quad \varphi^0 = \varphi_R^0 = 0 \quad (4)$$

and for L conversion

$$V^0 = V_L^0 = 1; \quad \varphi^0 = \varphi_L^0 = \pi \quad (5)$$

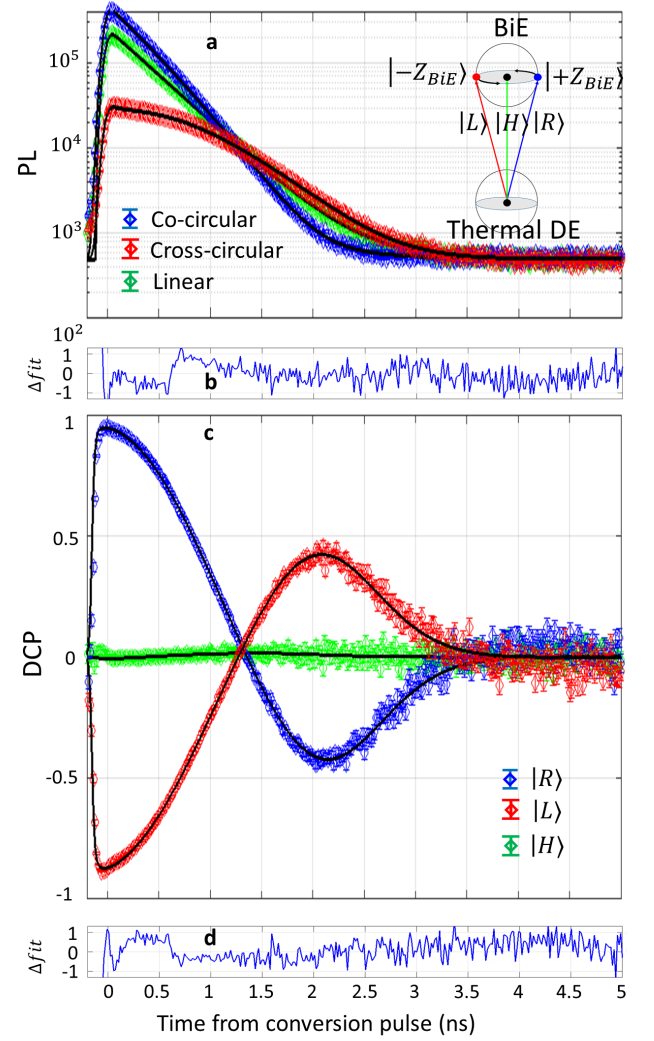


Figure 4. Experimental characterization of the BIE (excited DE) spin qubit. (a) Polarization-sensitive time-resolved PL measurement of the recombining BIE spectral line. Blue (red) diamond-marks represent PL, detected in a co- (cross-) circular-polarization to the polarization of the excitation and green diamond marks represent circularly polarized detection after linearly-polarized excitation. The color-matched solid lines represent the best model fits to the data using Eq. 10 and Eq. 11, with three fitting parameters: $T_{BIE} = 5.70 \pm 0.05 ns$, $T_2^* = 5.75 \pm 0.05 ns$, and $\tau_R = 0.39 \pm 0.01 ns$. (b) The difference between the fitted model and the measured co-circular polarization data normalized by the experimental uncertainty. (c) Time-resolved degree of circular polarization (DCP) of the PL for R, L, and H polarized excitations. (d) The difference between the fitted model and measured DCP for R excitation, normalized by the experimental uncertainty.

while for H conversion

$$V^0 = V_H^0 = \sqrt{(S_Y^0)^2 + (S_Z^0)^2}; \quad \varphi^0 = \varphi_H^0 = \arctan(S_Y^0/S_Z^0) \quad (6)$$

and for B conversion

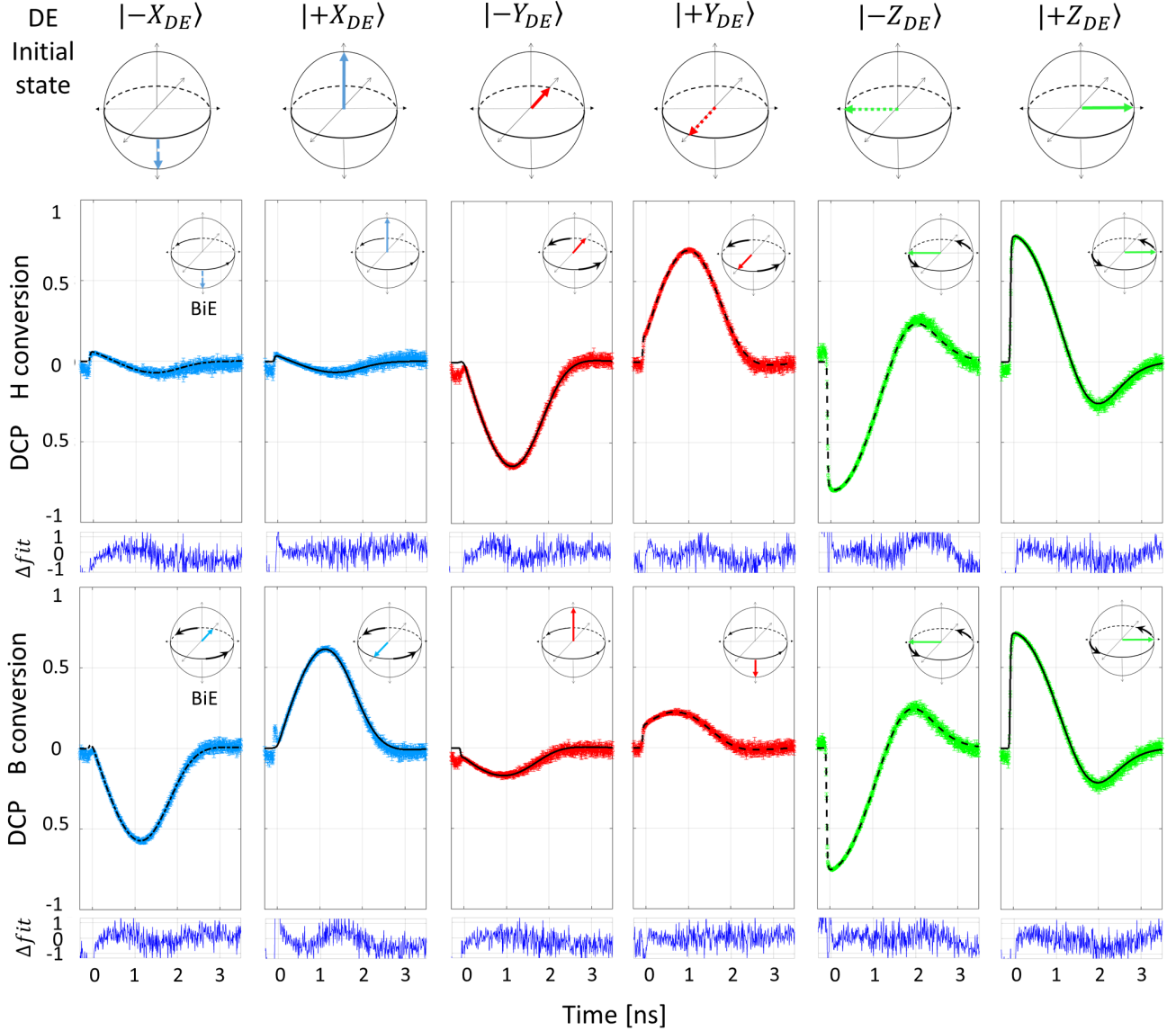


Figure 5. Full state tomography of the confined DE spin state for six different DE initializations, in 3 orthogonal bases. Blue, red and green arrows describe $|\pm X_{DE}\rangle$, $|\pm Y_{DE}\rangle$, and $|\pm Z_{DE}\rangle$ initializations on the top DE-Bloch-spheres. Below each Initialization's Bloch sphere, color-matched solid lines describe the measured time-resolved $DCP(t)$ followed H and B conversions. Overlaid solid black lines represent the best-fitted model using Eq. 12 to the measured data. The time-resolved differences between the fitted model and the measured DCP, normalized by the experimental uncertainty, are presented below each curve. The Bloch spheres in the insets describe the initial BiE spin state after the conversion and its temporal precession while it radiatively recombines.

$$V^0 = V_B^0 = \sqrt{(S_X^0)^2 + (S_Z^0)^2}; \quad \varphi^0 = \varphi_B^0 = \arctan(S_X^0/S_Z^0). \quad (7)$$

In addition to the natural coherent precession, the excited-qubit state undergoes decoherence [13, 38], which results in decay of the initial precession amplitude:

$$V_P(t) = V_P^0 \exp(-t^2/T_2^{*2}), \quad (8)$$

where $P=R, L, H$ or B and T_2^* is the dephasing-time of the excited-qubit. In addition, the excited-qubit decays radiatively while its spin-state precesses. Its photoluminescence (PL) emission intensity as a function of time is given by:

$$I(t) = I^0 \exp(-t/\tau_R), \quad (9)$$

where τ_R is its radiative lifetime and I^0 is the initial

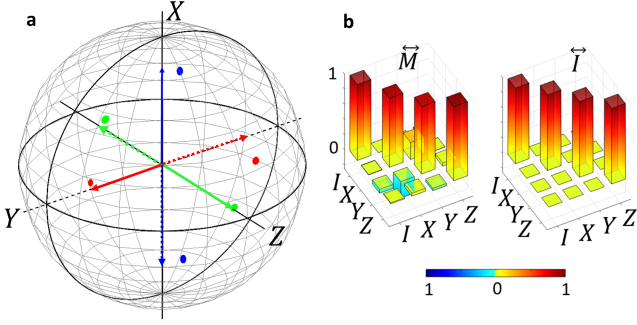


Figure 6. a) DE Bloch sphere, representing the initialized and measured states. Blue, red and green arrows represent $|\pm X_{DE}\rangle$, $|\pm Y_{DE}\rangle$ and $|\pm Z_{DE}\rangle$ DE initializations. The polarization degree is only 0.82 due to the finite efficiency of the optical depletion. The color-matched spots represent the tomographically measured states for each initialization. The spots volume represents one standard deviation of the measurement uncertainty. (b) Matrix representation (\vec{M}) of the state tomography measurement map. \vec{M} is a 4×4 positive-definite and trace-preserving map that maps an initialized state (corrected for the 0.82 initialization) into the measured one. The fidelity of the measured physical map, to the identity map (also shown in b), is 0.94 ± 0.02 .

emission intensity.

These three processes of Eqs.3-9 happen simultaneously, and thus the time dependent circularly polarized PL intensity of the excited-qubit can be described by:

$$I_R(t) = I^0 \exp(-t/\tau_R) \cdot [1 + V^0 \exp(-t^2/T_2^{*2}) \cos(-\frac{2\pi t}{T_{excited}} + \varphi^0)]/2 \quad (10)$$

and

$$I_L(t) = I^0 \exp(-t/\tau_R) \cdot [1 + V^0 \exp(-t^2/T_2^{*2}) \cos(-\frac{2\pi t}{T_{excited}} + \varphi^0 + \pi)]/2 \quad (11)$$

for right and left circularly polarized PL emission, respectively.

The time dependent degree of circular polarization (DCP) is defined as $DCP(t) = [I_R(t) - I_L(t)]/[I_R(t) + I_L(t)]$, therefore it is given by:

$$DCP_p(t) = V_P^0 \exp(-t^2/T_2^{*2}) \cdot \cos(-\frac{2\pi t}{T_{excited}} + \varphi_P^0) \quad (12)$$

Since $T_{excited}$ and T_2^{*2} can be measured independently, (see below), one can quite accurately obtain the four variables V_H^0 , V_B^0 , φ_H^0 and φ_B^0 , by fitting Eq. 12 to the measured time-dependent $DCP_p(t)$ resulting from the two converting pulses. These four variables accurately define the initial ground-level-qubit spin state as described by the three projections $[S_X^0, S_Y^0, S_Z^0]$ using EQs. 6-7.

We prefer to demonstrate the spin state tomography using the DE Π -system for two reasons:

(i) The DE and its BIE are an integer spin qubits, and even in the absence of external magnetic field the exchange interactions between the carriers remove the degeneracy between their spin up and spin down states [30, 39, 40]. Their eigenstates are described by $|\pm X_{DE}\rangle = (|+Z_{DE}\rangle \pm |-Z_{DE}\rangle)/\sqrt{2}$; and $|\pm X_{BIE}\rangle = (|+Z_{BIE}\rangle \pm |-Z_{BIE}\rangle)/\sqrt{2}$. The energy differences between the eigenstates are of an order of $1\mu\text{eV}$ which is smaller than the radiative width of the BIE optical transition ($\simeq 3\mu\text{eV}$) and much smaller than the spectral width of our laser pulse ($\simeq 100\mu\text{eV}$). Due to these splittings, the DE and the BIE precession times around the eigenstates' axis T_{DE} and T_{BIE} , are about an order of magnitude longer than the radiative time of the BIE.

(ii) Due to a small mixture between the bright exciton (BE) and dark exciton (DE) states, it is possible to initialize the DE spin state with high fidelity using a single optical pulse [32], just like the BE [26]. Initialization of the electron or the hole spin state is much more complicated [41, 42].

Another useful feature of the DE system is that the excitation and emission of the BIE occur at different wavelengths [30], preventing the laser light from blinding the PL detectors.

Fig. 4 describes the experiments used to characterize the BIE as a spin qubit. For the characterization measurements the DE is prepared in a thermal, totally mixed unpolarized state using a feeble continuous wave (CW) above-bandgap excitation (457nm) of the QD [13, 43]. A 12-ps-long resonantly tuned laser pulse then excites the DE to form a BIE. We use three different polarizations for the pulsed excitation: $|R\rangle$, $|L\rangle$, and $|H\rangle$. Since the DE-BIE is an optical Π -system, R- (L-) polarized pulse initializes the BIE in the $|+Z_{BIE}\rangle$ ($|-Z_{BIE}\rangle$) state, while H-polarized pulse results in a totally-mixed BIE state.

Following its photogeneration, the BIE evolves in time while it recombines radiatively. Using polarization-sensitive time-resolved PL measurements, one can readily obtain the BIE precession period (T_{BIE}), its dephasing time (T_2^*), and its radiative decay time (τ_R).

In Fig. 4a, we present the measured circularly polarized PL as a function of time after the pulsed excitation for three different cases. The blue (red) marks present PL, polarized Co-(cross-) circular to the excitation pulse, and the green line presents PL polarized both R and L, following an H-polarized pulse. The solid black lines present the best-fitted model of Eq. 10 and Eq. 11. For R- (L-) circularly polarized conversion pulse the initial BIE phase φ^0 is 0 (π) and the visibility V^0 is 1 (1). For the linear initialization $V^0 = 0$. In the last case, the PL simply decays radiatively. Therefore, this measurement is used to determine the radiative lifetime without any additional fitting parameters.

The BIE precession period and its dephasing are then fitted accurately using both the time-resolved PL measurements ($I_R(t)$ and $I_L(t)$) and $DCP(t)$ as presented in Fig. 4c. The measurements are fitted simultaneously and we obtain $T_{BIE} = 5.70 \pm 0.05\text{ns}$, $T_2^* = 5.75 \pm 0.05\text{ns}$

and $\tau_R = 0.39 \pm 0.01 ns$. As can be seen in Figs. 4b and d our fitting procedure agrees with all the measured data points within one standard deviation of the experimental uncertainty.

We now proceed by first depleting the QD from charges and from the remaining DE using a 7-ns-long optical pulse as described elsewhere [44]. We then write the DE spin state using a 12-ps optical π -pulse to an excited DE state [32]. About 100-ps later, we convert the DE into the BIE and then apply time-resolved circular polarization PL measurements to conclude the state tomography. This cycle is repeated at a 76 MHz rate.

Fig. 5 displays the results of these tomographic measurements. In Fig. 5, each DE initialization is described by an arrow on the Bloch sphere on the upper panel. $|\pm X_{DE}\rangle$, $|\pm Y_{DE}\rangle$ and $|\pm Z_{DE}\rangle$ initializations are represented by blue, red and green arrows respectively. The color-matched solid lines below each initialization represent the measured DCP as a function of time after the conversion for both H- and B- conversions. Black solid lines overlaid on the measured DCP represent the best-fitted model using Eq. 12. The differences between the fitted model and the measured DCP, normalized by the experimental uncertainty, are presented below each curve. The quality of the fits is evident since every measured point is within the experimental uncertainty from the calculated one. In the inset to each figure are schematic descriptions of the BIE spin state after the conversion pulse and its temporal evolution during its recombination.

One notes that for $|-X_{DE}\rangle$ and $|+X_{DE}\rangle$ initializations, the DCP for H-conversion is almost flat, which is not surprising since in these cases the BIE is formed in its $|\pm X_{BIE}\rangle$ eigenstates that do not evolve in time. Therefore it is nearly impossible to obtain φ^0 from these measurements. However, since B-polarized conversion transforms $|\pm X_{DE}\rangle$ to $|\pm Y_{BIE}\rangle$, which are coherent superpositions of the BiE eigenstates and thereby precess in time, the DCP is not flat and φ^0 can be easily obtained. For $|\pm Y_{DE}\rangle$ initializations, B converts $|\pm Y_{DE}\rangle$ to $|\mp X_{BIE}\rangle$, so the DCP signal is flat, while H converts $|\pm Y_{DE}\rangle$ to $|\pm Y_{BIE}\rangle$, so the DCP is not flat. For $|\pm Z_{DE}\rangle$ initializations, the DCP for both conversions is similar, because in both cases $|\pm Z_{DE}\rangle$ is converted to $|\pm Z_{BIE}\rangle$.

For each DE initialization, we determine the state by fitting the measured DCP curves of Fig. 5, for both H and B- conversions, to the model of Eq. 12. We note that only three fitting parameters $[S_X^0, S_Y^0, S_Z^0]$ are used to fit 12 time-resolved DCP(t) curves. Fig. 6a shows the

results of our fitting procedure, displayed on the DE Bloch sphere. Color-matched ovals represent one standard deviation of the experimental uncertainty of the measured-states, while color-matched arrows represent the six initialized-states. The length of the arrows represents the degree of polarization of the initializations, independently measured to be 0.82, due to the finite efficiency of the optical depletion [44].

Finally, we show in Fig. 6b the 4×4 \overleftrightarrow{M} matrix which maps the initialized DE state, represented by a 2×2 density matrix $\hat{\rho}_{init}$ to the DE state density matrix that we obtain by state tomography $\hat{\rho}_{tomog}$, or:

$$\hat{\rho}_{tomog} = \overleftrightarrow{M} \cdot \hat{\rho}_{init}.$$

We obtain the \overleftrightarrow{M} matrix from our measurements by finding the most probable positive and trace-preserving (physical) matrix that maps the six initial DE states to the measured ones in a similar procedure as described in Ref. [36]. The matrix that we obtain deviates from the expected 4×4 identity matrix \overleftrightarrow{I} , also shown in Fig. 6b for comparison. A fidelity of 0.94 ± 0.02 [45] quantifies the similarity between \overleftrightarrow{M} and \overleftrightarrow{I} . We attribute this deviation to the calibration accuracy of our liquid-crystal variable-retarder based polarization analyzers [32].

In summary, we demonstrate an all-optical measurement method for full state tomography of electronic spin qubits confined in semiconductor nanostructures. While previous methods, require the spin to be a part of an optical Λ -system, our method is more general since it relies on an optical Π -system, typical to long-lived confined electronic spins, such as conduction band electrons, valence-band holes, and dark excitons. The ability to perform full state tomography on electronic spins this way is essential for scaling up hybrid spin-multi photons graph-states, thereby constituting important step towards realizations of quantum information-based technologies.

ACKNOWLEDGMENTS

The support of the Israeli Science Foundation (ISF), and that of the European Research Council (ERC) under the European Union's Horizon 2020 research and innovation programme (Grant Agreement No. 695188) are gratefully acknowledged.

-
- [1] D. Loss and D. P. DiVincenzo, *Physical Review A* **57**, 120 (1998).
 - [2] D. P. DiVincenzo, *Fortschritte der Physik* **48**, 771 (2000).
 - [3] B. E. Kane, *Nature* **393**, 133 (1998).
 - [4] I. Bloch, *Nature* **453**, 1016 (2008).
 - [5] J. Clarke and F. K. Wilhelm, *Nature* **453**, 1031 (2008).

- [6] R. Hanson and D. D. Awschalom, *Nature* **453**, 1043 (2008).
- [7] H. J. Kimble, *Nature* **453**, 1023 (2008).
- [8] A. Imamoglu, D. D. Awschalom, G. Burkard, D. P. DiVincenzo, D. Loss, M. Sherwin, and A. Small, *Physical Review Letters* **83**, 4204 (1999).

- [9] N. Sangouard, C. Simon, H. de Riedmatten, and N. Gisin, *Reviews of Modern Physics* **83**, 33 (2011).
- [10] A. C. Johnson, J. R. Petta, J. M. Taylor, A. Yacoby, M. D. Lukin, C. M. Marcus, M. P. Hanson, and A. C. Gossard, *Nature* **435**, 925 (2005).
- [11] R. Blatt and D. Wineland, *Nature* **453**, 1008 (2008).
- [12] K. Saeedi, S. Simmons, J. Z. Salvail, P. Dluhy, H. Riemann, N. V. Abrosimov, P. Becker, H.-J. Pohl, J. J. L. Morton, and M. L. W. Thewalt, *Science* **342**, 830 (2013).
- [13] D. Cogan, O. Kenneth, N. H. Lindner, G. Peniakov, C. Hopfmann, D. Dalacu, P. J. Poole, P. Hawrylak, and D. Gershoni, *Physical Review X* **8** (2018), 10.1103/physrevx.8.041050.
- [14] R. Winik, D. Cogan, Y. Don, I. Schwartz, L. Gantz, E. R. Schmidgall, N. Livneh, R. Rapaport, E. Buks, and D. Gershoni, *Physical Review B* **95** (2017), 10.1103/physrevb.95.235435.
- [15] X.-L. Wang, Y.-H. Luo, H.-L. Huang, M.-C. Chen, Z.-E. Su, C. Liu, C. Chen, W. Li, Y.-Q. Fang, X. Jiang, J. Zhang, L. Li, N.-L. Liu, C.-Y. Lu, and J.-W. Pan, *Physical Review Letters* **120** (2018), 10.1103/physrevlett.120.260502.
- [16] H. Kosaka, T. Inagaki, Y. Rikitake, H. Imamura, Y. Mitsu-mori, and K. Edamatsu, *Nature* **457**, 702 (2009).
- [17] A. Morello, J. J. Pla, F. A. Zwanenburg, K. W. Chan, K. Y. Tan, H. Huebl, M. Möttönen, C. D. Nugroho, C. Yang, J. A. van Donkelaar, A. D. C. Alves, D. N. Jamieson, C. C. Escott, L. C. L. Hollenberg, R. G. Clark, and A. S. Dzurak, *Nature* **467**, 687 (2010).
- [18] P. Neumann, J. Beck, M. Steiner, F. Rempp, H. Fedder, P. R. Hemmer, J. Wrachtrup, and F. Jelezko, *Science* **329**, 542 (2010).
- [19] J. J. Pla, K. Y. Tan, J. P. Dehollain, W. H. Lim, J. J. L. Morton, F. A. Zwanenburg, D. N. Jamieson, A. S. Dzurak, and A. Morello, *Nature* **496**, 334 (2013).
- [20] T. Nakajima, M. R. Delbecq, T. Otsuka, P. Stano, S. Amaha, J. Yoneda, A. Noiri, K. Kawasaki, K. Takeda, G. Allison, A. Ludwig, A. D. Wieck, D. Loss, and S. Tarucha, *Physical Review Letters* **119** (2017), 10.1103/physrevlett.119.017701.
- [21] C. Kloeffel and D. Loss, *Annual Review of Condensed Matter Physics* **4**, 51 (2013).
- [22] O. Gywat, H. J. Krenner, and J. Berezovsky, *Spins in Optically Active Quantum Dots* (Wiley-VCH Verlag GmbH & Co. KGaA, 2009).
- [23] K. De Greve, P. L. McMahon, L. Yu, J. S. Pelc, C. Jones, C. M. Natarajan, N. Y. Kim, E. Abe, S. Maier, C. Schneider, M. Kamp, S. Höfling, R. H. Hadfield, A. Forchel, M. M. Fejer, and Y. Yamamoto, *Nature Communications* **4** (2013), 10.1038/ncomms3228.
- [24] W. B. Gao, P. Fallahi, E. Togan, J. Miguel-Sanchez, and A. Imamoglu, *Nature* **491**, 426 (2012).
- [25] K. De Greve, L. Yu, P. L. McMahon, J. S. Pelc, C. M. Natarajan, N. Y. Kim, E. Abe, S. Maier, C. Schneider, M. Kamp, S. Höfling, R. H. Hadfield, A. Forchel, M. M. Fejer, and Y. Yamamoto, *Nature* **491**, 421 (2012).
- [26] Y. Benny, S. Khatsevich, Y. Kodriano, E. Poem, R. Presman, D. Galushko, P. M. Petroff, and D. Gershoni, *Physical Review Letters* **106**, (2011).
- [27] M. Kroutvar, Y. Ducommun, D. Heiss, M. Bichler, D. Schuh, G. Abstreiter, and J. J. Finley, *Nature* **432**, 81 (2004).
- [28] D. Brunner, B. D. Gerardot, P. A. Dalgarno, G. Wüst, K. Karrai, N. G. Stoltz, P. M. Petroff, and R. J. Warburton, *Science* **325**, 70 (2009).
- [29] K. De Greve, P. L. McMahon, D. Press, T. D. Ladd, D. Bisping, C. Schneider, M. Kamp, L. Worschech, S. Höfling, A. Forchel, and Y. Yamamoto, *Nature Physics* **7**, 872 (2011).
- [30] E. Poem, Y. Kodriano, C. Tradonsky, N. H. Lindner, B. D. Gerardot, P. M. Petroff, and D. Gershoni, *Nature Physics* **6**, 993 (2010).
- [31] I. Schwartz, E. R. Schmidgall, L. Gantz, D. Cogan, E. Bordo, Y. Don, M. Zielinski, and D. Gershoni, *Physical Review X* **5**, (2015).
- [32] I. Schwartz, D. Cogan, E. R. Schmidgall, L. Gantz, Y. Don, M. Zielinski, and D. Gershoni, *Physical Review B* **92**, (2015).
- [33] E. Togan, Y. Chu, A. S. Trifonov, L. Jiang, J. Maze, L. Childress, M. V. G. Dutt, A. S. Sørensen, P. R. Hemmer, A. S. Zibrov, and M. D. Lukin, *Nature* **466**, 730 (2010).
- [34] N. H. Lindner and T. Rudolph, *Physical Review Letters* **103**, (2009).
- [35] S. E. Economou, N. Lindner, and T. Rudolph, *Physical Review Letters* **105** (2010), 10.1103/physrevlett.105.093601.
- [36] I. Schwartz, D. Cogan, E. R. Schmidgall, Y. Don, L. Gantz, O. Kenneth, N. H. Lindner, and D. Gershoni, *Science* **354**, 434 (2016).
- [37] G. Ramon, U. Mizrahi, N. Akopian, S. Braitbart, D. Gershoni, T. Reinecke, B. Gerardot, and P. Petroff, *Physical Review B* **73** (2006), 10.1103/physrevb.73.205330.
- [38] A. Bechtold, D. Rauch, F. Li, T. Simmet, P.-L. Ardelet, A. Regler, K. Müller, N. A. Sinitsyn, and J. J. Finley, *Nature Physics* **11**, 1005 (2015).
- [39] M. Bayer, G. Ortner, O. Stern, A. Kuther, A. A. Gorbunov, A. Forchel, P. Hawrylak, S. Fafard, K. Hinzer, T. L. Reinecke, S. N. Walck, J. P. Reithmaier, F. Klopfer, and F. Schäfer, *Physical Review B* **65**, (2002).
- [40] E. L. Ivchenko, *Optical Spectroscopy of Semiconductor Nanostructures* (Alpha Science, 2005).
- [41] M. Atature, *Science* **312**, 551 (2006).
- [42] A. J. Ramsay, S. J. Boyle, R. S. Kolodka, J. B. B. Oliveira, J. Skiba-Szymanska, H. Y. Liu, M. Hopkinson, A. M. Fox, and M. S. Skolnick, *Physical Review Letters* **100**, (2008).
- [43] Y. Benny, Y. Kodriano, E. Poem, D. Gershoni, T. A. Truong, and P. M. Petroff, *Physical Review B* **86**, (2012).
- [44] E. R. Schmidgall, I. Schwartz, D. Cogan, L. Gantz, T. Heindel, S. Reitzenstein, and D. Gershoni, *Applied Physics Letters* **106**, 193101 (2015).
- [45] R. Jozsa, *Journal of Modern Optics* **41**, 2315 (1994).